

Multifunctional passive metacrystals for enhancing wireless communications

¹Mohammad M. Asgari*, ²Peter B. Catrysse, ³Haiwen Wang, ²Shanhui Fan, and ¹Viktar Asadchy

¹Aalto University, Department of Electronics and Nanoengineering, Espoo 02150, Finland

²Stanford University, E. L. Ginzton Laboratory, Department of Electrical Engineering, Stanford, CA 94305, USA

³Stanford University, E. L. Ginzton Laboratory, Department of Applied Physics, Stanford, CA 94305, USA *mohammadmahdi.asgari@aalto.fi

Keywords: *Reconfigurable intelligent surfaces, smart skins, anomalous reflectors, multifunctional metasurfaces, inverse design, wireless communications*

Intelligent surfaces have emerged as a promising solution to enhance coverage and mitigate signal fading in future wireless communication systems, thereby improving bandwidth and data rates. Passive intelligent surfaces, in particular, demonstrate significant potential for reducing both energy consumption and operational costs. However, their current functionalities are typically constrained to operation within a single polarization, frequency band, and angle of arrival, limiting their applicability in realistic scenarios. In this work, we introduce volumetric dielectric composites, referred to as metacrystals, which are designed through computer optimization to greatly extend the capabilities of intelligent surfaces. Owing to their three-dimensional geometry, which supports a large number of degrees of freedom, metacrystals can simultaneously provide complex multiplexing responses for multiple signals. Each signal can be characterized by distinct parameters, including polarization, angle of incidence, frequency, and/or orbital angular momentum. The proposed metacrystals feature binarized permittivity contrast between low-permittivity materials and air gaps, and can thus be fabricated using filament-based additive manufacturing, supporting frequencies up to 100 GHz. By being cost-effective and scalable, these structures are well-suited for industrial applications, such as integration into building walls, where they can redirect or absorb signals in both indoor and outdoor environments with high versatility at millimeter-wave frequencies and beyond.

1 Introduction

The advent of sixth-generation (6G) and future wireless technologies will transform communications by offering higher data rates, improved energy efficiency, and lower latency [1]. However, the realization of high data rates necessitates the exploration of new frequency bands, such as millimeter (mm) waves and sub-THz bands [2, 3]. While these frequencies offer vast amounts of bandwidth, they also present considerable challenges due to their high atmospheric attenuation, free-space path loss, and harsher scattering effects when encountering obstacles [4]. Therefore, reliance on traditional multipath propagation is no longer feasible, and directional beams must be used for communication [1]. Moreover, higher-frequency signals are often blocked by obstacles such as walls, requiring a denser network of base stations and relays. Recently, metasurfaces, also referred to as intelligent surfaces, have been proposed to mitigate these challenges by efficiently redirecting communication signals in free space to bypass obstacles [5–8]. These artificial surfaces, strategically positioned on walls, ceilings, and even windows, can substantially enhance both indoor and outdoor signal coverage through anomalous reflection or refraction [9], requiring minimal to no energy for their operation.

Most of the existing studies on intelligent surfaces focused on achieving reconfigurable responses [8]. However, it has become evident that reconfigurable intelligent surfaces are currently too expensive for widespread adoption by the communication industry due to their need to operate at high frequencies (above 30-50 GHz), their large footprints (around a square meter), and the need for highly tunable constituent elements [9]. Consequently, their non-reconfigurable (completely passive) counterparts have recently gained great attention due to their significantly lower manufacturing and maintenance costs [9]. In fact, in many real-world scenarios, reconfigurability is not necessary because the positions of the receivers and transmitters are fixed or weakly varying. For instance, in industrial settings, machinery and sensors are usually installed in fixed locations; the infrastructure and major pathways in large public hubs remain constant; and in office environments, the locations of access points are typically fixed.

While several various pathways for the analytic design of passive intelligent surfaces were proposed (e.g., anomalous reflectors [10–12], smart skins [13], metagratings [14–16], and aperiodic gratings [17]), all of

them lack the sufficient versatility for realistic applications. Indeed, in most practical scenarios, it is necessary for the intelligent surface to operate effectively across both signal polarizations, multiple frequency bands, and various angles of arrival. However, realizing such versatile surfaces with the aforementioned techniques is extremely challenging, as these techniques rely on specific homogenization models (e.g., based on polarizability [18], susceptibility [19], or surface impedance tensors [20]). Factors such as frequency dispersion, nonlocality, and anisotropy make the implementation of the unit cells with required material parameters hardly possible. Furthermore, at millimeter-wave frequencies and above, parasitic effects become more significant, leading to parasitic capacitances and inductances in the circuit models of the unit cells [21]. Although several studies have attempted to address these issues, these approaches generally exhibit only one or two functionalities at a time due to the restricted number of degrees of freedom and reliance on analytical modeling [22–26].

In this paper, we propose the concept of *multifunctional* metacrystals as passive intelligent panels for wireless communications. We consider a *functionality* as an individual wavefront response specified for an incident beam with a distinct polarization, wavelength, and direction [27]. Hence, these metacrystals can simultaneously provide complex multiplexing responses for multiple signals, each characterized by its own set of parameters, including polarization, angle of incidence, frequency, and/or orbital angular momentum. For each illumination signal, the metacrystal can exhibit nearly arbitrary wave manipulation, including anomalous reflection and refraction, absorption, polarization conversion, and their combinations. This versatile functionality is achieved by transitioning from the traditional sub-wavelength single-layer metasurface design to a bulk multilayer topology with a larger number of degrees of freedom. We use the terminology “metacrystals” due to their similarity to both photonic crystals (supporting multiple diffraction orders) and metamaterials (with deeply sub-wavelength building blocks). To design the metacrystals, we employ an inverse design method using adjoint-based topology optimization [28] that was recently used for applications in fluid mechanics [29, 30], material science [31], acoustics [32] and optics [27, 28, 33–44]. This optimization approach provides a direct mapping from the desired electromagnetic response to the material topology, bypassing the need for homogenization models. As a proof of concept for future communications, we designed several reflective metacrystals engineered to perform various functionalities for different angles of arrival and two orthogonal polarizations within a single geometry. The designed metacrystals feature binarized permittivity contrast, consisting of regions with low-permittivity material and air gaps. This configuration allows for fabrication using conventional filament-based additive manufacturing technology [45–47], supporting high operational frequency ranges up to 100 GHz. Due to the inexpensive fabrication process, the metacrystals can be produced with large surface areas, making them suitable for industrial applications such as installation on building walls. We fabricated and experimentally characterized one of the designed metacrystals.

2 Results

2.1 Metacrystals for Wireless Communication

Passive intelligent surfaces in most realistic settings need to support multifunctional responses, providing desired and generally independent operations for several channels of incident signals. Indeed, wireless communication systems predominantly operate across a range of different frequency bands, necessitating network support for these bands. Signals may originate from various transmitters and have random or specific polarizations and directions of arrival. With our multifunctional metacrystals, we aim to implement such multiplexed responses into a single material platform. In general, the concept of metacrystals can be applied to both transmissive and reflective geometries. However, in this work we concentrate on the latter scenario as typically intelligent surfaces are deployed on top of opaque walls of the buildings, preventing signal transmission.

Figure 1 depicts one possible scenario of the implementation of the multifunctional metacrystals for indoor communication. Naturally, the concept can also be equally useful for outdoor communications. In the considered scenario of office space, there are three transmitters (e.g., Wi-Fi routers) and 2 receivers

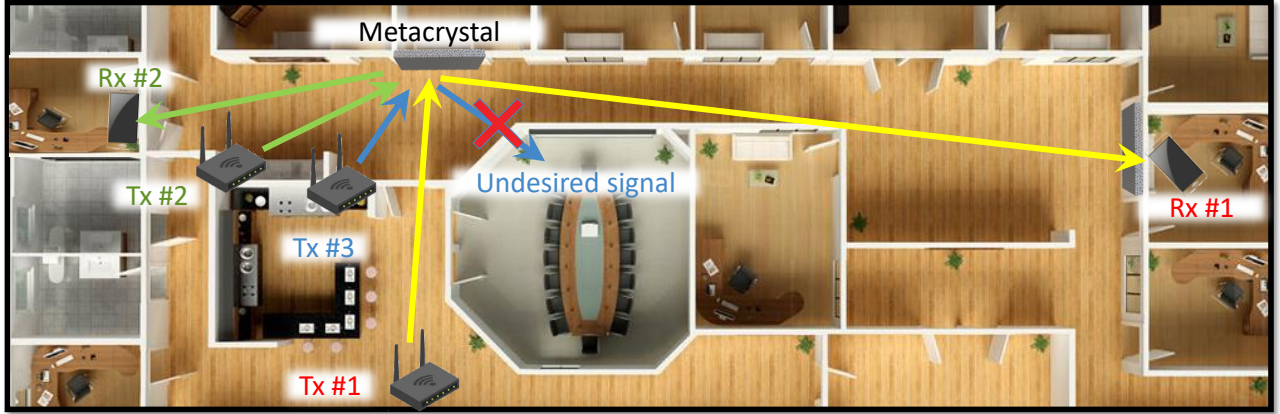


Figure 1: Schematic of the possible scenario for using multifunctional metacrystals to optimize the wireless network in an office environment.

(e.g., mobile phones) that need to communicate. The signal from transmitter Tx #1 is set to be redirected by the metacrysal toward receiver Rx #1. At the same time, the signal from Tx #2, positioned at a different location from Tx #1 and generally operating at a different frequency band, must be efficiently reflected toward Rx #2. Moreover, we aim that for Tx #3, the metacrysal behaves as an ideal absorber, preventing any parasitic reflections, especially toward the meeting space in the middle of Fig. 1. Although traditional design approach would require three separate intelligent surfaces to cover the specified functionalities, the proposed metacrysal can replace them all, saving the deployment footprint, minimizing the material use, and avoiding possible interference problems.

In what follows, we assume all signals (incident and reflected) propagate in the same incidence plane. This assumption allows us to design metacrystals with two-dimensional geometry, as shown in Fig. 2. Here, the metacrysal has spatial variations in two dimensions (xz -plane) but remains uniform in the third dimension along the y -axis (corresponding to the out-of-plane direction in Fig. 1). Nevertheless, the same concept could be extended to metacrystals with three-dimensional geometries supporting multiple incidence planes. Moreover, we assume that the metacrysal is periodic in one direction with period D . The periodicity plays a double role. On the one hand, due to the discrete translational symmetry of the metacrysal, its operation is relatively robust to possible displacements in space of the transmitters ΔS_{Tx} and/or receivers ΔS_{Rx} , as shown in Fig. 2 with cyan arrows (assuming their orientations do not change). In contrast, aperiodic intelligent surfaces are typically more sensitive to such displacements because they are designed for the exact locations of the receiver and transmitter [13, 48, 49]. Thus, metacrystals, despite their non-reconfigurable nature, can accommodate certain variables in wireless communication environment. On the other hand, the metacrysal's periodicity allows us to significantly reduce the simulation domain for accelerating the optimization. Furthermore, with periodic structures, it is easier to tile them and align to cover larger surface areas if required.

The period D of the metacrysal plays an important role. Not only does it provides the possibility to diffract the incident beams towards non-specular directions (so-called anomalous reflection [10, 18, 50]), it also allows us to discretize the angular space into Bloch diffraction orders, depicted by dashed lines in Fig. 2. For wide-beam illuminations with narrow incident wavevector spectra (plane-wave approximation), the diffraction angle $\theta_{r,n}$ of the n -th Bloch order is given by $k_{\text{inc}} \sin \theta_{r,n} = k_{\text{inc}} \sin \theta_{\text{inc}} + 2\pi \frac{n}{D}$, where $k_{\text{inc}} = \omega/c$ is the incident wave number, c is the speed of light, and θ_{inc} is the incident angle. In most previous works on intelligent surfaces, the period was on the order of the wavelength of incident signals $\lambda = 2\pi/k_{\text{inc}}$, which allows only three diffraction channels, that is, $n = 0, \pm 1$ [12]. Such sparse distribution of diffraction orders is insufficient for practical scenarios where multiple transmitters or receivers are present (see an example in Fig. 1). Therefore, in this work, we capitalize on the large spatial periods on the order of multiple wavelengths. Once the angular directions toward the transmitters and receivers are known, we choose a sufficiently large period so that these directions approximately overlap with open diffraction orders. While further increasing the periodicity would improve the discretization

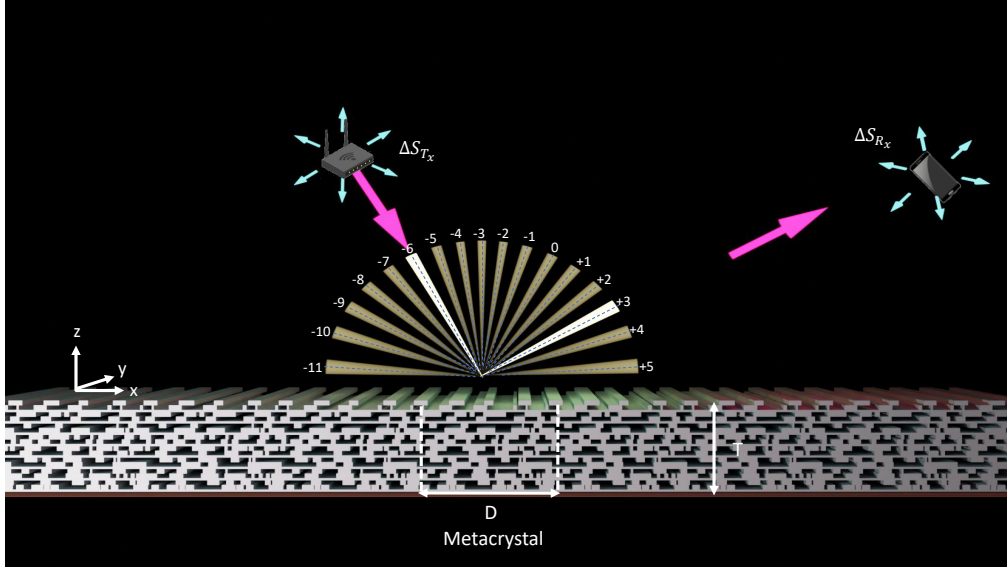


Figure 2: Illustration of a metacrystal with one-dimensional periodicity D and thickness T . It has an optimized spatially nonuniform distribution of permittivity in the xz -plane, while it features uniform geometry along the y -direction. The periodicity is large enough so that the metacrystal supports a significant number of diffraction orders n , which are enumerated by integers. These diffraction orders effectively discretize the angular space, enabling the routing of signals from transmitters to receivers whose locations can be nearly arbitrary. In this particular case, the incident signal is reflected in the $n = 3$ diffraction order which corresponds to the receiver's direction. Due to the translational symmetry of the metacrystal, its operation is relatively robust to possible displacements in space of the transmitter ΔS_{T_x} and receiver ΔS_{R_x} (shown with the cyan arrows). The yellow cones depict the finite-width diffracted beams scattered by the metacrystal (due to the finite spatial extent of the metacrystal). The power carried by each beam is determined by the unit-cell design. The structure rendered is the designed metacrystal whose performance is described in Fig. 4(b).

of the angular space and ultimately make the overlap perfect, in practice, such densification is not necessary. This is because the metacrystal is always finite in the plane parallel to its surface, meaning that scattered beams always have small but finite angular widths. Therefore, it is sufficient to discretize the angular space to a finite number of diffraction channels, as shown in Fig. 2.

2.2 Demonstrators

In this section, we aim to showcase two demonstrator examples of multifunctional metacrystals. As discussed above, to effectively discretize the angular space in the xz -plane, we need to allow a sufficiently large number of diffraction orders. Without the loss of generality, we choose a periodicity of $D = 4.2\lambda$, which enables us to achieve 9 diffraction channels for normal incidence or 8 and 9 for the considered oblique illuminations. For the first demonstrator, we require lossless operation and consider 6 functionalities chosen arbitrarily (but respecting energy conservation and reciprocity) that must be satisfied simultaneously. In this example, the permittivity of the materials is assumed to be purely real. The 6 functionalities are shown in Fig. 3(a) using three incidence planes (blue, green, and red) separated along the y -direction for visual clarity. In each plane, the desired routing of waves for two polarizations (TE and TM) is shown. We aim that for incident signals at 0° , the TE and TM polarizations are reflected into the $n = +4$ and $n = +1$ diffraction channels, respectively, as indicated with yellow and purple arrows in Fig. 3(a). This configuration corresponds to a polarization-selective anomalous reflection splitter. On the other hand, for an incident angle of 20° , the TE (white arrow) and TM (green arrow) signals are directed towards positive and negative diffraction channels, that is, the $n = +2$ and $n = -4$ channels, respectively. For the last two functionalities, we require polarization-independent anomalous reflection towards the -1 -st diffraction order when TE and TM signals are incident at 45° . Importantly, the incident angles (0° , 20° , and 45°) were chosen completely arbitrarily. This example thus illustrates that we can select the angles of arrival from different transmitters independently.

For the optimization, we discretize the metacrystal unit cell into a finite amount of voxels in the xz -plane

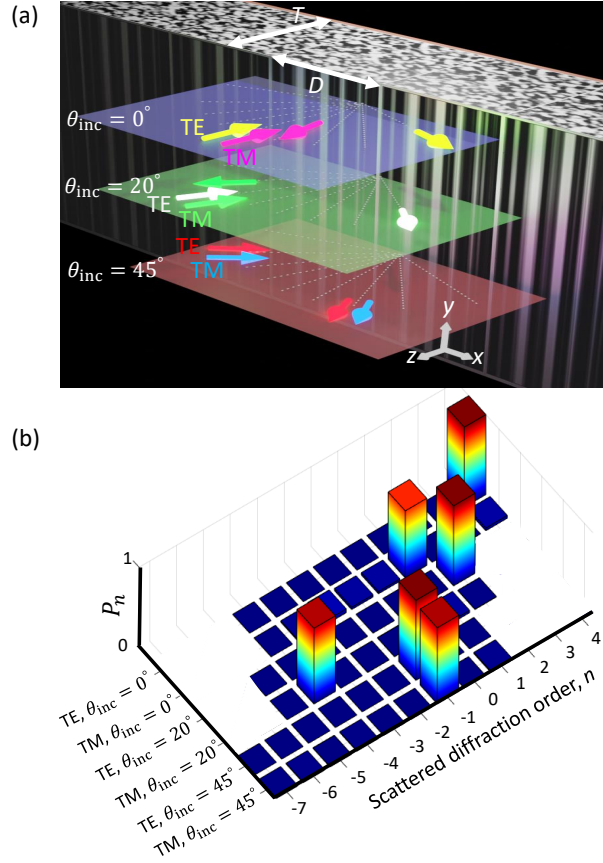


Figure 3: (a) The optimized topology of the first demonstrator metacrytal providing simultaneously 6 functionalities for TE and TM signals incident at 0° , 20° , and 45° . For visual clarity, each pair of functionalities is depicted in a separate incidence plane (the metacrytal is uniform along the y -direction). Arrows of different colors denote different illumination scenarios. The thin dashed black lines depict the diffraction order directions for a given incidence. (b) The simulated distribution of the reflected power into different diffraction channels for the 6 incidence scenarios. Due to the lossless metacrytal response, the total sum of reflected power for each incidence is equal to unity. The blank spaces in the plot correspond to closed (evanescent) diffraction orders. The reflection angle of the n -th diffraction order can be determined according to $\theta_{r,n} = \arcsin(\sin \theta_{\text{inc}} + n\lambda/D)$.

and adjust their permittivities to achieve the desired multifunctional response. For the first demonstrator, we choose the number of voxels in the z - and x -directions to be 70 and 150, respectively, to ensure a high-efficiency response of the final metacrytal. With the voxel dimensions $t = 0.168\lambda$ and $d = 0.028\lambda$, this translates into the total thickness of $T = 11.76\lambda$ and period $D = 4.2\lambda$. Here, we assume the grayscale permittivity distribution with $\varepsilon_{\text{max}} = 5$, which is a realistic value for low-loss dielectrics in the considered mm-wave frequency band. To understand how different metacrytal parameters influence the optimization of its response, we refer the reader to Supplementary Material where we performed a corresponding systematic study. The optimized topology of the metacrytal can be seen in Fig. 3(a). Although its total thickness is large compared to the wavelength, its absolute value is only 7.1 cm for an operational frequency of 50 GHz. Such metacrytals could be readily deployed on internal or external walls of buildings, appearing as nothing more than futuristic passive panels that slightly protrude from the wall profile. The permittivity distribution of the metacrytal at all voxels is detailed in the Supplementary Data. The power distribution across the reflected diffraction channels for the optimized metacrytal is calculated using rigorous coupled wave analysis (RCWA) and plotted in Fig. 3(b). A clear pattern is evident with the near-unity-amplitude columns, signifying the highly efficient reflection of six incident waves into the designated reflection channels. The reflected powers for $\theta_{\text{inc}} = 0^\circ$ reach $P_{+4}^{\text{TE}} = 99.99\%$ and $P_{+1}^{\text{TM}} = 83.92\%$, for $\theta_{\text{inc}} = 20^\circ$, we obtain $P_{+2}^{\text{TE}} = 99.99\%$ and $P_{-4}^{\text{TM}} = 94.63\%$, and for $\theta_{\text{inc}} = 45^\circ$, $P_{-1}^{\text{TE}} = 99.99\%$ and $P_{-1}^{\text{TM}} = 95.24\%$. The overall efficiency for the six functionalities calculated as the arithmetic average of the reflected powers specified above reaches an impressive 95.62%, showcasing the

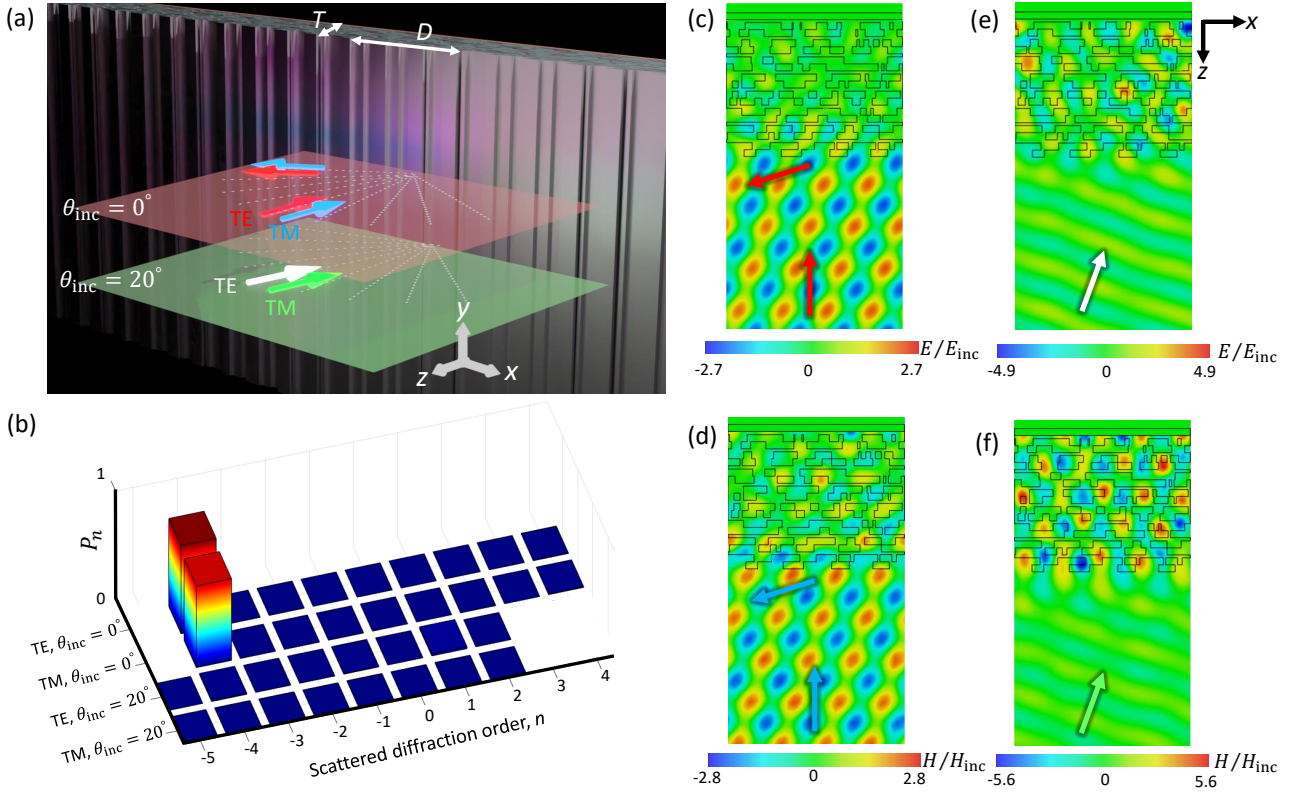


Figure 4: (a) The optimized topology of the second demonstrator metacrytal providing simultaneously 4 functionalities for TE and TM signals incident at 0° and 20° . For visual clarity, each pair of functionalities is depicted in a separate incidence plane. Arrows of different colors denote different illumination scenarios. The thin dashed black lines depict the diffraction order directions for a given incidence. (b) The simulated distribution of the reflected power into different diffraction channels for the 4 incidence scenarios. The blank spaces in the plot correspond to closed (evanescent) diffraction orders. For two incident scenarios, the metacrytal absorbs nearly all the incident power, as evidenced by the minimal overall reflection. (c)–(f) The simulated total fields (sum of incident and reflected fields) for four illumination scenarios.

effectiveness and precision of the designed method. As is seen from Fig. 3(b), the parasitic scattering to other diffraction channels is negligible. For the second demonstrator, our objective is to fabricate and experimentally characterize the proposed metacrytal. To streamline the experimental verification, which involves complex angular-resolved measurements of the far fields for each incidence scenario, we limit the number of functionalities to four. The desired response of the second demonstrator metacrytal is shown in Fig. 4(a). In this setup, we require polarization-insensitive response, as it is essential in many practical situations. Achieving polarization-insensitive response is non-trivial and requires comparable structural complexity as in the scenario where different polarizations experience different prescribed functionalities [23, 24]. The TE and TM signals normally incident onto the metacrytal must be anomalously reflected into the $n = -4$ diffraction channel, corresponding to a reflected angle of 72° . On the other hand, all signals incident at $\theta_{\text{inc}} = 20^\circ$ must be completely absorbed by the metacrytal. This functionality could be useful in scenarios like the one shown in Fig. 1 to avoid possible parasitic interferences (see the blue arrows). To significantly simplify the fabrication process, we optimized the metacrytal using a binarized permittivity distribution (see details in the Experimental Section). This approach enables us to use only one material during fabrication, with a permittivity of $\epsilon_{\text{max}} = 2.2$, which alternates spatially with air gaps having a permittivity of $\epsilon_{\text{min}} = 1$. This configuration facilitates straightforward fabrication using 3D printers, particularly the most common and cost-effective filament-based printers. The mentioned permittivity value was experimentally determined for the low-loss material used in the fabrication, polyacrylic acid (UltiMaker PLA of silver color), as explained in Experimental Section. The measured loss tangent of the material is $\tan \delta = 0.01$. The smallest feature size of the designed metacrytal, obtained by applying the blur function, was $0.056\lambda = 0.34 \text{ mm}$, which is well within the accuracy range of commercial 3D printers. To

ensure structural integrity and maintain interconnection among all voxels, we added thin homogeneous layers (with 0.336λ thickness) between each two layers of optimized voxels in the z -direction. The optimized structure comprised only 16 voxel layers, each with a thickness of $t = 0.168\lambda$. Combined with the homogeneous structural layers with 0.071λ , the total thickness was $T = 3.26\lambda$. Other parameters, D , t , and d are the same as in the first demonstrator.

The geometry of the optimized second demonstrator is shown in Fig. 4(a), with a view of the xz plane provided in Fig. 2. The permittivity distribution of the metacrystal at all voxels can be found in the Supplementary Data. The multifunctional response of the metacrystal simulated using RCWA is shown in Fig. 4(b). The designed structure exhibits anomalous reflection efficiencies of 84.39% for TE polarization and 78.26% for TM polarization for normally incident signals. Remarkably, despite being composed of a low-loss dielectric backed by a ground plane, the same structure nearly fully absorbs both polarizations at an incident angle of 20° , with absorption rates of 90.47% and 96.34% for TE and TM polarizations, respectively.

Furthermore, in Figs. 4(c)–(f), we present the normalized electric field distributions for TE-polarized incidences and the magnetic field distributions for TM-polarized incidences across the four illumination scenarios. The data were obtained using CST Studio Suite. Notably, in the anomalous reflection scenarios, almost no field hot spots are generated within the optimized metacrystal, and the total field outside it exhibits a partially standing-wave pattern due to the superposition of the normally incident plane wave and the single plane wave reflected at 72° . Conversely, in the full absorption scenarios depicted in Figs. 4(d),(f), strong field hot spots are generated inside the crystal, leading to the high absorption. The total fields outside the metacrystal are predominantly characterized by a single incident plane wave, indicating minimal parasitic scattering into open diffraction channels. The average efficiency of the second metacrystal demonstrator reaches 80%, which is an impressive result, especially considering the challenges posed by permittivity blurring and binarization due to fabrication limitations, the small overall thickness, and the presence of uniform layers for structural integrity.

The fabricated sample of the second demonstrator (see Fig. 5(b)) comprises 8 unit cells along the x axis and has the size of $33.6\lambda = 20.16$ cm, $10.5\lambda = 6.3$ cm, and $3.26\lambda = 1.95$ cm along the x , y , and z directions, respectively. Since the operational frequency of the metacrystal is 50GHz, characterizing it using quasi-optical setups, such as those in [51], is particularly challenging. This is because Gaussian beams must be very wide (with a small span in momentum space) to resolve the sharp angular response of the metacrystal. Therefore, the operation of the fabricated metacrystal was verified by measurements in an anechoic chamber emulating the free-space environment (see more details in the Experimental Section). In this case, due to the large distance between the transmitting antenna and the sample under test, the incident wavefront can be well approximated as planar. However, since the entire surface of the metacrystal is illuminated, it is crucial to account for edge scattering effects when evaluating its efficiency. To address this, we employ the measurement method proposed in [10, 52].

The schematic of the experimental setup can be seen in Fig. 5(a). Two sets of experiments were performed to validate the demonstrator functionality for four incidences. In the first set of experiments, we measured the anomalous reflection of normally incident waves toward the -4 -th diffraction order for both TE and TM polarizations. The orientation and position of the platform with the metacrystal and the transmitting antenna were fixed. The receiving antenna was moved around the metacrystal at a fixed distance from it, always facing the metacrystal (see Fig. 5(a)). First, we measured the received signal at the desired -4 -th diffraction order. For waves at 50 GHz, we observed that the maximum of the diffracted peak occurred at $\theta_r = 76^\circ$, which slightly deviates from the theoretical angle of 72° , likely due to fabrication imperfections in the printed sample. Next, we measured the received signal in the reference case where the metacrystal was replaced by a metal plate of the same dimensions tilted at an angle $\theta_r/2 = 38^\circ$ (to ensure a strong specularly reflected signal). Using these two measurements and the theory based on the physical optics approximation (see the Experimental Section and Supplementary Material), we determine the anomalous-reflection efficiency of the metacrystal for both polarizations, as plotted in Fig. 5(c). At a frequency of $f_{\text{op}} = 49.475$ GHz (shown with dashed vertical line), the measured efficiency ξ_r reaches values of 70.2% and 66.3% for the TE and TM polarized waves, respectively, with peak values of 72.8%

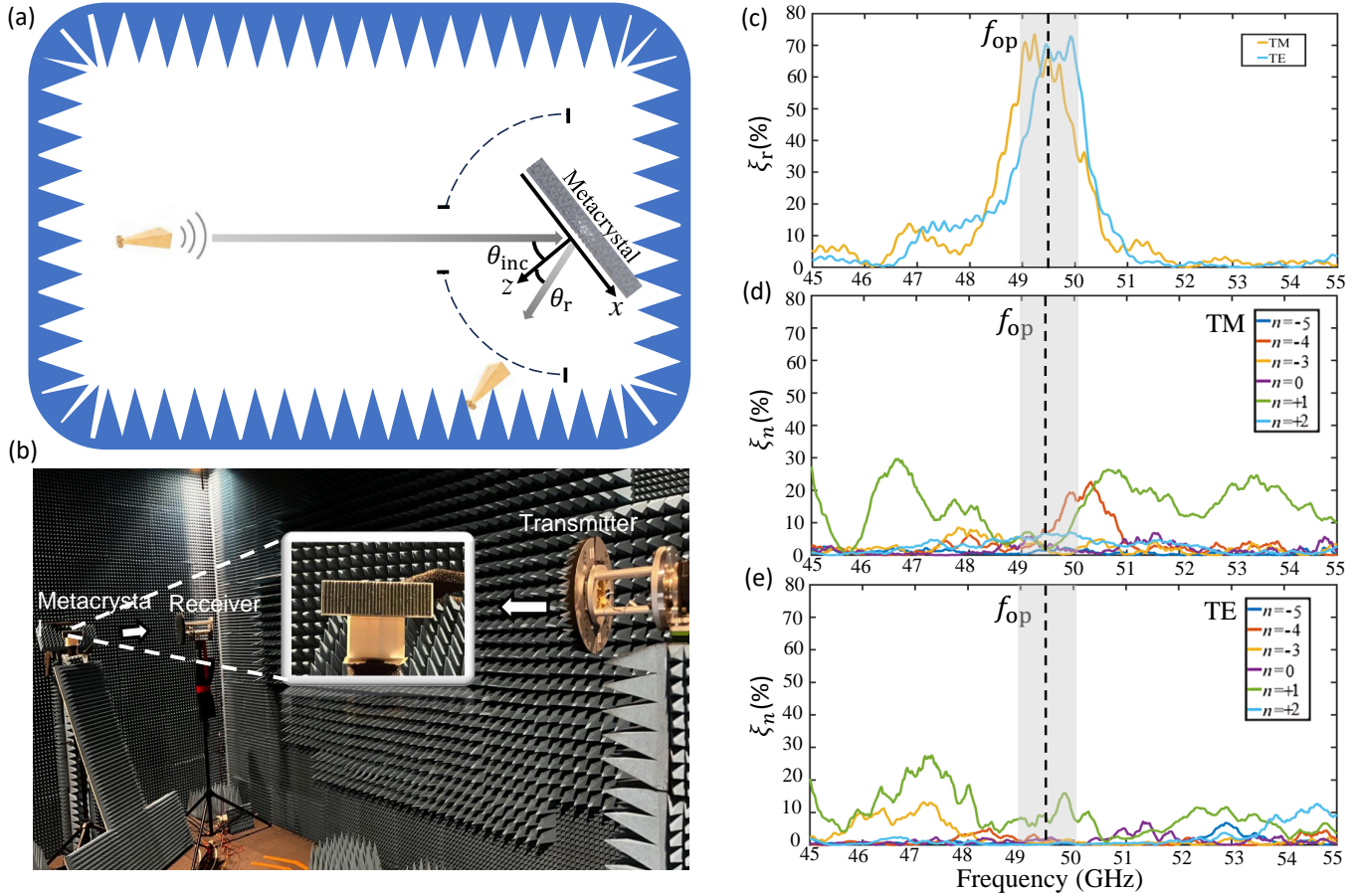


Figure 5: (a) The schematic of the experimental setup. (b) Experimental setup in an anechoic chamber with the inset depicting the zoomed-in image of the metacrystal sample. (c) The efficiency of the anomalous reflection for TE and TM polarized waves incident normally onto the sample. The dashed vertical line depicts the operational frequency f_{op} . The grey shaded regions denote the half-power bandwidth for anomalous reflection functionality. (d) The parasitic scattering efficiency ξ_n across different diffraction channels for TM polarized waves incident at an angle $\theta_{inc} = 20^\circ$ onto the sample. At frequency f_{op} , the overall parasitic scattering is small, confirming the high absorption exhibited by the sample. (e) Same as in (d) for TE polarization.

and 73.4% for TE and TM at slightly different frequencies of 49.91 GHz and 49.24 GHz, respectively. This is slightly lower than the simulated values 84.4% and 78.3% reported above, likely due to fabrication imperfections and the approximation of physical optics used to account for the finite size of the metacrystal. From Fig. 5(c), one can observe the operational bandwidth of the metacrystal for anomalous reflection of approximately 2% (shown with grey shaded region). Outside this bandwidth, the metacrystal continues to exhibit strong anomalous reflection, but the reflection angle deviates from the desired value, causing the receiving antenna, which is fixed in position, to fail to detect the reflected power. In the second set of experiments, we measured the absorption characteristics of the metacrystal when it was illuminated at an angle of $\theta_{\text{inc}} = 20^\circ$. To evaluate the absorption level, we measured the parasitic scattering from the metacrystal into multiple open diffraction channels. For each diffraction channel, a reference measurement was also performed using a metal plate (as described earlier) to determine the parasitic scattering efficiency, ξ_n , for a given channel n . The measured parasitic scattering is plotted in Figs. 5(d) and (e) for TM and TE polarizations, respectively. In these measurements, the receiving antenna was positioned in the direction of a given diffraction channel n calculated at operational frequency f_{op} (for each diffraction channel). This way, the absorption efficiency can be calculated as $\xi_a = 1 - \sum_n \xi_n$, but only at frequencies close to f_{op} . Indeed, during the frequency sweep, the positions of the diffraction channels continuously shift and do not overlap with the location of the receiving antenna. As seen from Figs. 5(d) and (e), for frequencies close to f_{op} , parasitic scattering is strongly suppressed, confirming high absorption efficiency. The absorption efficiencies at f_{op} for both polarizations (dashed vertical lines in Figs. 5(d) and (e)) reach impressive values of $\xi_a^{\text{TE}} = 87.52\%$ and $\xi_a^{\text{TM}} = 78.24\%$, respectively. It is worth noting that due to the physical obstruction caused by the receiving antenna, we were unable to measure parasitic scattering into two diffraction orders, $n = -1$ and $n = -2$. However, scattering into these directions is expected to be minimal according to the simulated data. A comparison between the experimental and simulated results for the absorption scenario at the operating frequency can be found in the Supplementary Material.

Finally, when considering the four functionalities in the experimental setup, the efficiencies are reported as $\xi_r^{\text{TE}} = 70.2\%$, $\xi_r^{\text{TM}} = 66.3\%$, $\xi_a^{\text{TE}} = 87.5\%$, and $\xi_a^{\text{TM}} = 78.2\%$. The overall average efficiency is calculated to be 74.9% at f_{op} .

3 Conclusion

We present a novel approach for the simultaneous manipulation of multiple wave properties, with significant potential to impact a broad range of applications and systems. We demonstrated the effectiveness of this approach through the design, fabrication, and measurement of a multifunctional metacrystal. This method holds great promise for enhancing wireless communication, particularly by enabling the development of passive intelligent surfaces that address coverage challenges in mm-wave and THz communications. By employing a binarized topology, our approach is fully compatible with additive manufacturing, which makes it scalable, cost-effective, and suitable for mass production, with the potential for widespread use in wireless communication networks. Additionally, the generic nature of our method enables others to build upon this work and explore new opportunities in wireless communication systems.

4 Experimental Section

Topology Optimization:

We discretize the metacrystal in the xz -plane into deeply subwavelength voxels with different permittivity values within a specific range $\varepsilon \in [\varepsilon_{\text{min}}; \varepsilon_{\text{max}}]$. The optimized region in the two-dimensional simulation is the unit cell with dimension (D, T) in the (x, z) directions, respectively. The design parameters being optimized are the relative permittivity values of each voxel. The design process aims to minimize the fol-

lowing loss function:

$$\text{LF} = \sum_{i,n,k} \left| R_{i,n,k}^{\text{obj}} - R_{i,n,k}^{\text{act}} \right|^2, \quad (1)$$

where R represents the reflectivity (intensity ratio) into a given diffraction order, i is the index introduced to differentiate between various incidences (e.g., $i = 1, 2, \dots, 6$ for the scenario shown in Fig. 3, as the metacrystal is optimized for six different incident waves in total), n denotes the diffraction order index, and k indicates the polarization (either TE or TM). The indices “obj” and “act” refer to the objective and actual calculated reflectivity values, respectively.

We employ RCWA to calculate the reflection and subsequently assess the loss function as described in Eq. (1). Gradients are derived using the autograd package [28]. Binarized permittivity distributions (as shown, for example, in Fig. 2) are achieved through the projection method [53], where the density functions are initialized with random coherent noise [41]. The optimization typically converges after 70 to 500 iterations. Additional details can be found in [42].

Additionally, we implement a blur function to control the minimum feature size of the structure and to smoothen the permittivity distribution [54]

Device Fabrication:

Applying the bi-level topology optimization, we generated a 2D binary permittivity distribution of the metacrystal. The data were imported into COMSOL Multiphysics. Leveraging MATLAB LiveLink scripts, we then extracted a 3D model and generated the corresponding .stl file. The .stl file was then imported into Ultimaker Cura 5.3.1 for final device preparation. The finalized file was uploaded to the Ultimaker S5, and printer settings were optimized to achieve the best possible print quality. The printing process for the final structure took 34 hours and used 18.17 meters of silver-colored PLA. A 0.25 mm nozzle was used to achieve higher resolution in the xy-plane, which increased the printing time. By selecting a 0.4 mm nozzle and a 0.1 mm layer thickness, the printing time could be reduced to 25 hours.

Permittivity Characterization:

We used polyacrylic acid (UltiMaker PLA of silver color) for the fabrication of our metacrystal. Since the permittivity of this PLA had not been previously measured in the millimeter-wave frequency range, we performed its measurements using the method proposed in [55], which is particularly suited for this frequency range. A uniform test sample printed using Ultimaker S5 3D printer was placed between the flanges of two WR-10 waveguides. This method is advantageous because it does not require the sample cross-section to precisely match the waveguide aperture, which is beneficial given the small dimensions of the aperture. For the measurements of the S-matrix, we used a vector network analyzer with frequency extenders. The system was calibrated using the Thru-Reflect-Line (TRL) method.

Far-Field Measurements:

Far-field measurements were conducted in an anechoic chamber using a vector network analyzer connected to both transmitting and receiving horn antennas. The antennas used in this experiment were dual-polarized probes (AYSOL, model ASY-CWG-D-400-UG383). They operate in the frequency range of 40 GHz to 60 GHz and support dual polarization, allowing measurements in both horizontal and vertical polarizations. The antennas shown in Fig. 5(a)–(b) provided a gain of approximately 13.0 dBi at 50 GHz. The metacrystal was located at a distance of 5.69 m (around 95λ) from the transmitting antenna, where the radiation from the antenna can be approximated as a plane wave. The distance between the metacrystal and the receiving antenna was fixed to 1.75 m (around 29λ). To control the metacrystal orientation, it was attached to a platform rotating around the y -axis. The reflected signal from the metacrystal, indicated by $|S_{21,m}|$, was measured by the receiving antenna for various angles θ_r . In the reference experiments, the metacrystal was replaced with a metallic plate of the same dimensions without altering the surrounding environment. We tilted the metallic plate by an angle $\theta_r/2$ and measured the reflected wave, $|S_{21,p}|$, toward the same angle θ_r (the two antennas had the same positions in both measurements). To calculate the efficiency of the anomalous reflection from the metacrystal, we additionally calculate the correction factor ξ_0 which essentially denotes the ratio of the far-field scattered fields in a given direction from a metal plate and an ideal metacrystal [10, 52]. Importantly, $\xi_0 \neq 1$ since the

ideal metacrystal and metal plate have different receiving and scattering effective apertures despite equal physical dimensions. Coefficient ξ_0 depends on θ_{inc} and θ_r and is calculated for both TE and TM in the Supplementary Information. The efficiency of the anomalous reflection of the metacrystal is given by:

$$\xi_r = \frac{1}{\xi_0} \frac{|S_{21,m}|}{|S_{21,p}|}. \quad (2)$$

Supporting Information

Supporting Information is available from the Wiley Online Library or from the author.

Acknowledgements

We acknowledge the computational resources provided by the Aalto Science-IT project. S. F. acknowledges the support of a MURI project from the U. S. Air Force Office of Scientific Research (Grant No. FA9550-21-1-0244). V.A. acknowledges the Research Council of Finland and DoD (Project No. 365679), Finnish Foundation for Technology Promotion, and Research Council of Finland Flagship Programme, Photonics Research and Innovation (PREIN), decision number 346529, Aalto University. Furthermore, we extend our appreciation to Dr. Xuchen Wang for his invaluable assistance with the permittivity measurements and electromagnetic software simulations. We would also like to express our sincere gratitude to Dr. Francisco S. Cuesta, Mr. Javad Shabanpour, Mr. Mostafa Movahhedi, and Ms. Shadi Safaei Jazi for their support during the experimental phase.

References

- [1] Mostafa Zaman Chowdhury, Md Shahjalal, Shakil Ahmed, and Yeong Min Jang. 6g wireless communication systems: Applications, requirements, technologies, challenges, and research directions. *IEEE Open Journal of the Communications Society*, 1:957–975, 2020.
- [2] Xiong Wang, Linghe Kong, Fanxin Kong, Fudong Qiu, Mingyu Xia, Shlomi Arnon, and Guihai Chen. Millimeter wave communication: A comprehensive survey. *IEEE Communications Surveys & Tutorials*, 20(3):1616–1653, 2018.
- [3] Ian F Akyildiz, Josep Miquel Jornet, and Chong Han. Terahertz band: Next frontier for wireless communications. *Physical communication*, 12:16–32, 2014.
- [4] Theodore S Rappaport, Robert W Heath Jr, Robert C Daniels, and James N Murdock. *Millimeter wave wireless communications*. Pearson Education, 2015.
- [5] Nadège Kaina, Matthieu Dupré, Geoffroy Lerosey, and Mathias Fink. Shaping complex microwave fields in reverberating media with binary tunable metasurfaces. *Scientific reports*, 4(1):6693, 2014.
- [6] Ertugrul Basar, Marco Di Renzo, Julien De Rosny, Merouane Debbah, Mohamed-Slim Alouini, and Rui Zhang. Wireless communications through reconfigurable intelligent surfaces. *IEEE access*, 7:116753–116773, 2019.
- [7] George C Alexandropoulos, Geoffroy Lerosey, Mérouane Debbah, and Mathias Fink. Reconfigurable intelligent surfaces and metamaterials: The potential of wave propagation control for 6g wireless communications. *arXiv preprint arXiv:2006.11136*, 2020.
- [8] Saber Hassouna, Muhammad Ali Jamshed, James Rains, Jalil ur Rehman Kazim, Masood Ur Rehman, Mohammad Abualhayja, Lina Mohjazi, Tei Jun Cui, Muhammad Ali Imran, and Qammer H Abbasi. A survey on reconfigurable intelligent surfaces: Wireless communication perspective. *IET Communications*, 17(5):497–537, 2023.
- [9] Roberto Flamini, Danilo De Donno, Jonathan Gambini, Francesco Giuppi, Christian Mazzucco, Angelo Milani, and Laura Resteghini. Toward a heterogeneous smart electromagnetic environment for millimeter-wave communications: An industrial viewpoint. *IEEE Transactions on Antennas and Propagation*, 70(10):8898–8910, 2022.
- [10] Ana Díaz-Rubio, Viktor S Asadchy, Amr Elsakka, and Sergei A Tretyakov. From the generalized reflection law to the realization of perfect anomalous reflectors. *Science advances*, 3(8):e1602714, 2017.
- [11] Alex M. H. Wong and George V. Eleftheriades. Perfect anomalous reflection with a bipartite Huygens’ metasurface. *Phys. Rev. X*, 8:011036, Feb 2018.
- [12] Fu Liu, Do-Hoon Kwon, and Sergei Tretyakov. Reflectarrays and metasurface reflectors as diffraction gratings: A tutorial. *IEEE Antennas and Propagation Magazine*, 2023.
- [13] Giacomo Oliveri, Paolo Rocca, Marco Salucci, and Andrea Massa. Holographic smart em skins for advanced beam power shaping in next generation wireless environments. *IEEE Journal on Multiscale and Multiphysics Computational Techniques*, 6:171–182, 2021.
- [14] Younes Ra’di, Dimitrios L Sounas, and Andrea Alù. Metagratings: Beyond the limits of graded metasurfaces for wave front control. *Physical review letters*, 119(6):067404, 2017.

- [15] Oshri Rabinovich and Ariel Epstein. Analytical design of printed circuit board (pcb) metagratings for perfect anomalous reflection. *IEEE Transactions on Antennas and Propagation*, 66(8):4086–4095, 2018.
- [16] Vladislav Popov, Fabrice Boust, and Shah Nawaz Burokur. Controlling diffraction patterns with metagratings. *Physical Review Applied*, 10(1):011002, 2018.
- [17] Yongming Li, Xikui Ma, Xuchen Wang, Grigori Ptitsyn, Mostafa Movahediqomi, and Sergei A Tretyakov. All-angle scanning perfect anomalous reflection by using passive aperiodic gratings. *IEEE Transactions on Antennas and Propagation*, 2023.
- [18] Viktor S Asadchy, Mohammad Albooyeh, Svetlana N Tsvetkova, Ana Díaz-Rubio, Younes Ra’di, and Sergei A Tretyakov. Perfect control of reflection and refraction using spatially dispersive metasurfaces. *Physical Review B*, 94(7):075142, 2016.
- [19] Guillaume Lavigne, Karim Achouri, Viktor S Asadchy, Sergei A Tretyakov, and Christophe Caloz. Susceptibility derivation and experimental demonstration of refracting metasurfaces without spurious diffraction. *IEEE Transactions on Antennas and Propagation*, 66(3):1321–1330, 2018.
- [20] Do-Hoon Kwon. Lossless scalar metasurfaces for anomalous reflection based on efficient surface field optimization. *IEEE Antennas and Wireless Propagation Letters*, 17(7):1149–1152, 2018.
- [21] David M Pozar. *Microwave engineering: theory and techniques*. John Wiley & sons, 2021.
- [22] Xuchen Wang, Ana Diaz-Rubio, Huanan Li, Sergei A Tretyakov, and Andrea Alu. Theory and design of multifunctional space-time metasurfaces. *Physical Review Applied*, 13(4):044040, 2020.
- [23] Yuval Shklarsh and Ariel Epstein. Semianalytically designed dual polarized printed-circuit-board (pcb) compatible metagratings. *IEEE Transactions on Antennas and Propagation*, 2023.
- [24] Fengming Hu and Ariel Epstein. Cavity-excited metagrating antennas with controlled frequency diverse patterns. In *2023 IEEE International Symposium on Antennas and Propagation and USNC-URSI Radio Science Meeting (USNC-URSI)*, pages 1251–1252. IEEE, 2023.
- [25] Sharon Elad and Ariel Epstein. Simultaneous polarization conversion and anomalous reflection with anisotropic printed-circuit-board (pcb) metagratings. *arXiv preprint arXiv:2407.05648*, 2024.
- [26] Xiujian Zou, Youming Zhang, Ruoyu Lin, Guangxing Gong, Shuming Wang, Shining Zhu, and Zhenlin Wang. Pixel-level bayer-type colour router based on metasurfaces. *Nature Communications*, 13(1):3288, 2022.
- [27] David Sell, Jianji Yang, Sage Doshay, Rui Yang, and Jonathan A Fan. Large-angle, multifunctional metagratings based on freeform multimode geometries. *Nano letters*, 17(6):3752–3757, 2017.
- [28] Weiliang Jin, Wei Li, Meir Orenstein, and Shanhui Fan. Inverse design of lightweight broadband reflector for relativistic lightsail propulsion. *ACS Photonics*, 7(9):2350–2355, 2020.
- [29] Cetin B Dilgen, Sumer B Dilgen, David R Fuhrman, Ole Sigmund, and Boyan S Lazarov. Topology optimization of turbulent flows. *Computer Methods in Applied Mechanics and Engineering*, 331:363–393, 2018.
- [30] Martin Philip Bendsoe and Ole Sigmund. *Topology optimization: theory, methods, and applications*. Springer Science & Business Media, 2013.
- [31] Cyrill Bösch. *Topological Matter by Inverse Design*. PhD thesis, ETH Zurich, 2024.
- [32] Rasmus E Christiansen, Fengwen Wang, and Ole Sigmund. Topological insulators by topology optimization. *Physical Review Letters*, 122(23):234502, 2019.
- [33] Topology optimization for nano-photonics. *Laser & Photonics Reviews*, 5(2):308–321, 2011.
- [34] Alexander Y Piggott, Jesse Lu, Konstantinos G Lagoudakis, Jan Petykiewicz, Thomas M Babinec, and Jelena Vučković. Inverse design and demonstration of a compact and broadband on-chip wavelength demultiplexer. *Nature photonics*, 9(6):374–377, 2015.
- [35] Tyler W Hughes, Momchil Minkov, Ian AD Williamson, and Shanhui Fan. Adjoint method and inverse design for nonlinear nanophotonic devices. *ACS Photonics*, 5(12):4781–4787, 2018.
- [36] Raphaël Pestourie, Carlos Pérez-Arancibia, Zin Lin, Wonseok Shin, Federico Capasso, and Steven G Johnson. Inverse design of large-area metasurfaces. *Optics express*, 26(26):33732–33747, 2018.
- [37] Nasim Mohammadi Estakhri, Brian Edwards, and Nader Engheta. Inverse-designed metastructures that solve equations. *Science*, 363(6433):1333–1338, 2019.
- [38] Philip Camayd-Muñoz, Conner Ballew, Gregory Roberts, and Andrei Faraon. Multifunctional volumetric meta-optics for color and polarization image sensors. *Optica*, 7(4):280–283, 2020.
- [39] Yannick Augenstein and Carsten Rockstuhl. Inverse design of nanophotonic devices with structural integrity. *ACS photonics*, 7(8):2190–2196, 2020.
- [40] Rasmus E Christiansen and Ole Sigmund. Inverse design in photonics by topology optimization: tutorial. *JOSA B*, 38(2):496–509, 2021.
- [41] Nathan Zhao, Peter B. Catrysse, and Shanhui Fan. Perfect rgb-ir color routers for sub-wavelength size cmos image sensor pixels. *Advanced Photonics Research*, 2(3):2000048, 2021.
- [42] Haiwen Wang, Weiliang Jin, Cheng Guo, Nathan Zhao, Sean P Rodrigues, and Shanhui Fan. Design of compact meta-crystal slab for general optical convolution. *ACS Photonics*, 9(4):1358–1365, 2022.

- [43] Peter B Catrysse, Nathan Zhao, Weiliang Jin, and Shanhui Fan. Subwavelength bayer rgb color routers with perfect optical efficiency. *Nanophotonics*, 11(10):2381–2387, 2022.
- [44] Gregory Roberts, Conner Ballew, Tianzhe Zheng, Juan C Garcia, Sarah Camayd-Muñoz, Philip WC Hon, and Andrei Faraon. 3d-patterned inverse-designed mid-infrared metaoptics. *Nature Communications*, 14(1):2768, 2023.
- [45] Vasileios G Ataloglou and George V Eleftheriades. Synthesis of modulated dielectric metasurfaces for precise antenna beam-forming. *Physical Review Applied*, 19(4):044033, 2023.
- [46] Wei-Ren Ng, Dathon R Golish, Hao Xin, and Michael E Gehm. Direct rapid-prototyping fabrication of computer-generated volume holograms in the millimeter-wave and terahertz regime. *Optics express*, 22(3):3349–3355, 2014.
- [47] Xi-Pu Dong, Jie-Rong Cheng, Fei Fan, Shi-Tong Xu, Xiang-Hui Wang, and Sheng-Jiang Chang. Wideband sub-thz half-wave plate using 3d-printed low-index metagratings with superwavelength lattice. *Optics express*, 27(1):202–211, 2019.
- [48] Svetlana N Tsvetkova, Viktor S Asadchy, and Sergei A Tretyakov. Scanning characteristics of metamirror antennas with sub-wavelength focal distance. *IEEE Transactions on Antennas and Propagation*, 64(8):3656–3660, 2016.
- [49] Sembiam R Rengarajan. Scanning and defocusing characteristics of microstrip reflectarrays. *IEEE Antennas and Wireless Propagation Letters*, 9:163–166, 2010.
- [50] Nanfang Yu, Patrice Genevet, Mikhail A Kats, Francesco Aieta, Jean-Philippe Tetienne, Federico Capasso, and Zeno Gaburro. Light propagation with phase discontinuities: generalized laws of reflection and refraction. *science*, 334(6054):333–337, 2011.
- [51] Xuchen Wang, Ana Díaz-Rubio, Viktor S Asadchy, Grigorii Ptitsyn, Andrey A Generalov, Juha Ala-Laurinaho, and Sergei A Tretyakov. Extreme asymmetry in metasurfaces via evanescent fields engineering: Angular-asymmetric absorption. *Physical Review Letters*, 121(25):256802, 2018.
- [52] VS Asadchy, Ana Díaz-Rubio, SN Tsvetkova, D-H Kwon, Amr Elsakka, Mohamed Albooyeh, and SA Tretyakov. Flat engineered multichannel reflectors. *Physical Review X*, 7(3):031046, 2017.
- [53] Fengwen Wang, Boyan Stefanov Lazarov, and Ole Sigmund. On projection methods, convergence and robust formulations in topology optimization. *Structural and multidisciplinary optimization*, 43:767–784, 2011.
- [54] Tyler W Hughes, Ian AD Williamson, Momchil Minkov, and Shanhui Fan. Forward-mode differentiation of maxwell’s equations. *ACS Photonics*, 6(11):3010–3016, 2019.
- [55] Xuchen Wang and Sergei A Tretyakov. Fast and robust characterization of lossy dielectric slabs using rectangular waveguides. *IEEE Transactions on Microwave Theory and Techniques*, 70(4):2341–2350, 2022.